J. Fluid Mech. (2011), *vol.* 684, *pp.* 227–250. © Cambridge University Press 2011
doi:10.1017/jfm.2011.298

Dynamics of a deformable, transversely rotating droplet released into a uniform flow

Eric K. W. Poon[1,2], Shaoping Quan[1]†, Jing Lou[1], Matteo Giacobello[3] and Andrew S. H. Ooi[2]

[1] Institute of High Performance Computing, 1 Fusionopolis Way, No. 16-16 Connexis, Singapore 138632, Singapore

[2] Department of Mechanical Engineering, University of Melbourne, Parkville, Victoria 3010, Australia

[3] Air Vehicles Division, Defence Science and Technology Organisation, 506 Lorimer Street, Fishermans Bend, Victoria 3207, Australia

(Received 13 November 2010; revised 24 June 2011; accepted 5 July 2011; first published online 30 August 2011)

The effects of transverse rotation on the dynamics of a droplet released into a uniform free stream are numerically investigated. The range of the dimensionless rotation rate is limited to $0 \leqslant \Omega^* \leqslant 1$, to avoid any possibility of the droplet breaking up. Droplet dynamics and deformations undergo distinct changes when the dimensionless rotational rate (Ω^*) reaches a critical value. The critical rotational rate $\Omega_{crit}{}^*$ is sensitive to the change in the density ratio, but less dependent on the viscosity ratio and interfacial tension. Below $\Omega_{crit}{}^*$, the droplet drag coefficients are reduced marginally as the effect of the rotation is quickly suppressed by the free stream. Above $\Omega_{crit}{}^*$, the drag coefficients decrease initially as the rotation effect dominates at earlier times, resulting in a global minimum. The drag coefficients increase monotonically at later times, when the rotation effects decrease and the free-stream effects become dominant. The only exception is with the increase in the viscosity ratio and the surface tension, which either inhibits droplet deformation or restores the droplet to a more spherical shape in the late stages of droplet evolution. The droplet also experiences lift due to the effects of the transverse rotation. It is observed that the lift coefficients are less dependent on the droplet frontal area as the lift is generated by the velocity difference between the upper and lower interface. In general, the lift coefficients increase with Ω^* at earlier times and decrease at later times as the difference in the velocity between the upper and lower interface decreases. In some extreme cases, the lift coefficients even become negative.

Key words: drops and bubbles

1. Introduction

The transport of a liquid droplet is a rapidly growing research area with numerous potential engineering and medical applications. One of the most ubiquitous technologies is inkjet printing. Conventionally, inkjets have been used for paper printing only. But with the development of a better designed nozzle, inkjets have been applied to the printing of biomolecules such as DNA and antibodies (Khan *et al.* 2008). Recently, scientists have begun to induce rotation on droplets, by either

† Email address for correspondence: quansp@ihpc.a-star.edu.sg

https://doi.org/10.1017/jfm.2011.298 Published online by Cambridge University Press

vibrating the nozzle at particular frequencies (Tan, Teo & Hu 2008) or with the introduction of the Coriolis force (Haeberle *et al.* 2006), to control the trajectory of the droplet in order to achieve more desirable results. It is demonstrated that droplet rotation leads to three-dimensional chaotic mixing regions, in which mixing occurs through the stretching and folding of material lines. It also offers control of both the size and location of chaotic mixing within the droplet (Chabreyrie *et al.* 2010). Other areas in which the transport of a liquid droplet is of interest include chemical mixing (Chabert, Dorfman & Viovy 2005), cell encapsulation (He *et al.* 2005) and combustion in engines. Droplet rotation can substantially affect droplet evaporation and combustion efficiency (Pearlman & Sohrab 1991), which has been adopted in rotating spray atomisers or fuel injection. In view of the above considerations, detailed understanding of the underlying physics of a rotating droplet travelling in a crossflow is necessary to improve the design, efficiency and accuracy of nozzles or fuel injectors.

It is well known that a rotating rigid spherical body experiences a 'Robin–Magnus' lift force as it travels in a free stream, and a number of studies have been performed to predict this force. In contrast, detailed knowledge about a deformable, rotating droplet in a free-stream flow is still lacking. Some of the pioneering studies of a deformable, rotating droplet were performed in a stationary matrix. The study began when Newton explained the flattening of the earth as a fluid medium, due to its rotation. However, much of our knowledge of rotating droplets came from Plateau (1863) who experimentally identified a sequence of bifurcations as a droplet begins to rotate. More recently Chandrasekhar (1965), using the method of moments, studied the natural frequency of a rotating droplet undergoing different types of perturbation. He discovered a critical rotation rate at which the rotating droplet bifurcates into a two-lobed shape. This stability analysis was further extended by Brown & Scriven (1980). Busse (1984), by neglecting viscous damping effects and assuming small oscillations as well as incorporating linear theory, derived analytical solutions for the frequency shift of a rotating droplet for both axisymmetric and asymmetric modes of oscillations. These analytical solutions, together with the energy equations by Lamb (1945), were later used by Lee, Lyell & Wang (1985) to derive an equation for the viscous damping of an oscillating and rotating droplet. They found that for an asymmetric oscillation mode, droplet rotation does not affect viscous damping. In contrast, viscous damping was shown to be highly dependent on the mode of an axisymmetric oscillation.

Although analytical solutions are frequently adapted by different researchers, their validity has been the subject of discussion for decades. Annamalai, Trinh & Wang (1985) experimentally studied the oscillations of a rotating droplet. They concluded that Busse's solutions provided a satisfactory prediction of frequency shift at $\Omega < \omega_o/2$, but overestimated the results otherwise. Here, ω, subscript o and Ω represent the natural frequency of the droplet, the mode of oscillation and the rotation speed, respectively. The discrepancy was again proved by Watanabe (2008), who performed numerical simulations on a spherical droplet subjected to an initial solid-body rotation. The validity of the critical rotation rate predicted by Chandrasekhar (1965) had also been questioned by Wang *et al.* (1986) and Biswas, Leung & Trinh (1991). By using an acoustic levitation in both Spacelab (outer space) and ground-based environments, they showed that the critical rotation rate predicted by Chandrasekhar was higher than the experimental data. However, Rhim, Chung & Elleman (1988), by employing another levitation technique, were able to match the theoretical critical rotation rate. The critical rotation rate was finally verified by Wang *et al.* (1994) in a zero-gravity environment during a space flight. They explained that the discrepancy between previous experiments and Chandrasekhar's prediction was due

https://doi.org/10.1017/jfm.2011.298 Published online by Cambridge University Press

to the acoustic flattening of the droplet. The effect of gravity on the bifurcation point observed by Wang *et al.* (1994) had also led to another Spacelab study by Lee *et al.* (1998).

The studies mentioned above were all performed in a situation where the external fluid is stationary. In addition, traditional studies of a rotating liquid droplet in a crossflow usually assumed that the droplet remains spherical. This is based on the assumption that the Weber number is small. However, experimental (Hsiang & Faeth 1992) and numerical (Quan & Schmidt 2006) studies have shown that the droplet behaviour can be substantially modified by its deformation. Although interest has been shown in diverse disciplines, difficulties in setting up the apparatus experimentally (Wang *et al.* 1994) and handling large deformations on the interface numerically have restricted study of a highly deformable droplet. In this study a moving mesh interface tracking method (MMIT), coupled with local mesh adaptation developed by Quan & Schmidt (2007), is employed to study the dynamics of a deformable, transversely rotating droplet released into a uniform flow field. In § 2, a brief overview of the governing equations, jump and continuity conditions across the interface, and mesh adaption method is described. Detailed descriptions of the numerical formulations have been presented in previous investigations (Dai *et al.* 2002; Perot & Nallapati 2003; Dai & Schmidt 2005; Quan & Schmidt 2007). Code validation is performed against a rotating droplet in a stationary matrix and is presented in § 3. The effects of non-dimensional rotating rates, viscosity ratio, density ratio and initial Weber numbers on the droplet dynamics are presented in § 4. Conclusions are drawn in § 5.

2. Numerical formulation

2.1. *Numerical method*

The three-dimensional motion of an incompressible, immiscible, Newtonian-fluid liquid droplet is described by the Navier–Stokes equations. In this study, the integral form of the Navier–Stokes equations are solved in a discretised stream-function formulation using a finite volume staggered mesh method (Perot & Nallapati 2003), thus automatically ensuring the mass conservation (Perot & Nallapati 2003). The present method also allows implementation of the exact fractional step method (Chang, Giraldo & Perot 2002), and as a result, the Poisson equation is dropped. The face flux and the cell-centre velocity is then constructed from Stokes' theorem and Gauss's divergence theorem. Readers are referred to Chang *et al.* (2002), Perot & Nallapati (2003) and Quan & Schmidt (2007) for details of the numerical scheme and discretisation method.

In our method, the viscous and convection terms are advanced using a Crank–Nicolson scheme, whereas the time advancement is via a three-step, second-order, low-storage Runge–Kutta scheme (Perot & Nallapati 2003). The stability of the solution is governed by Courant–Friedrichs–Lewy number (CFL), surface tension criterion and the mesh Péclet number Pe, as described in Quan & Schmidt (2007). The time step used in the present study is the minimum of the time steps calculated from the three criteria above.

2.2. *Interface tracking scheme*

Accuracy in simulating an incompressible and immiscible two-phase flow relies heavily on the interface tracking method. At present, there are two major categories of numerical method for the multiphase flow: the diffuse-interface method and the sharp-interface approach. The diffuse-interface method includes the volume of fluid

https://doi.org/10.1017/jfm.2011.298 Published online by Cambridge University Press

method (DeBar 1974; Youngs 1982), level set method (Osher & Fedkiw 2001; Sethian & Smereka 2003), front-tracking method (Unverdi & Tryggvason 1992), the lattice Boltzmann method (Zheng, Shu & Chew 2006) and the immersed boundary method (Li & Lai 2001). These methods solve the Navier–Stokes equations on a fixed mesh. The drawback of these methods lies with the handling of the interface. The fluid and interface properties for these methods are usually smoothed by some defined functions across a finite set of grid points.

The boundary integral method (Youngren & Acrivos 1976) and the MMIT method (Quan & Schmidt 2007; Quan, Lou & Schmidt 2009*a*; Quan 2011) fall into the sharp-interface method category. Both methods treat the interface as having zero thickness, which means that the boundary conditions (often referred to as the jump conditions) at the interface are implemented directly without smoothing. However, the use of a boundary integral method has been limited to Stokes flow thus far, and the accuracy of the MMIT method can be hampered in the absence of mesh adaptation. To overcome this, local mesh adaptation schemes have been successfully coupled with MMIT to provide high-fidelity numerical data for a wide range of multiphase flows (Quan & Schmidt 2006, 2007). Another challenge for MMIT is to deal with topological transitions, but this challenge has been recently addressed by Quan *et al.* (2009*a*) and Quan (2011).

The simulations reported in this paper utilise the MMIT method to locate the interface. The MMIT method requires a set of boundary conditions across the interface to satisfy the discontinuity conditions. Further details are provided in the Appendix. Throughout the simulation, the interfaces move in a Lagrangian manner to conserve mass and to avoid mixing. However, the interior nodes are able to move freely in order to maintain good mesh quality. The quality of the mesh, Q, is checked against the criteria of Knupp (2003),

$$Q_f = \frac{\sqrt{3}A_f}{l_{11}+l_{22}-l_{12}} \quad \text{and} \quad Q_C = \frac{3(V_C\sqrt{2})^{2/3}}{\frac{3}{2}(l_{11}+l_{22}-l_{33})-(l_{12}+l_{23}+l_{13})} \tag{2.1}$$

where l_{ij}, $i,j=1,2,3$, are elements of a metric tensor calculated from the Jacobian matrix at each node of the cell (Knupp 2003), A and V denote the surface area of an equilateral triangle and the volume of an equilateral tetrahedron, respectively, subscript f and C represent the face and cell, respectively. The Jacobian matrix contains information about the shape, surface and volume of the cell. Therefore, the quality metrics essentially compare the area/volume ratio of an equilateral triangle/tetrahedron to that of an arbitrary one, with a value of one indicating that the element is equilateral, while a value of zero suggests that the element is degenerated. Unlike the body-fitted/arbitrary Lagrangian–Eulerian method (ALE) (Feng, Hu & Joseph 1994; Swaminathan, Mukundakrishnan & Hu 2006), where a grid regeneration scheme was employed to remesh the computational domain when the quality of the mesh deteriorates, the MMIT method utilised a mesh adaptation scheme locally when needed. Details of the mesh adaptation scheme can be obtained in Dai & Schmidt (2005) and Quan & Schmidt (2007).

3. Problem setup and code validation

3.1. *Initial and boundary conditions*

Figure 1 presents the coordinate system and the computational domain for the flow situation investigated. A spherical droplet of radius R_i with an initial angular velocity, Ω, in the x-direction is subjected to a sudden acceleration by a uniform

https://doi.org/10.1017/jfm.2011.298 Published online by Cambridge University Press

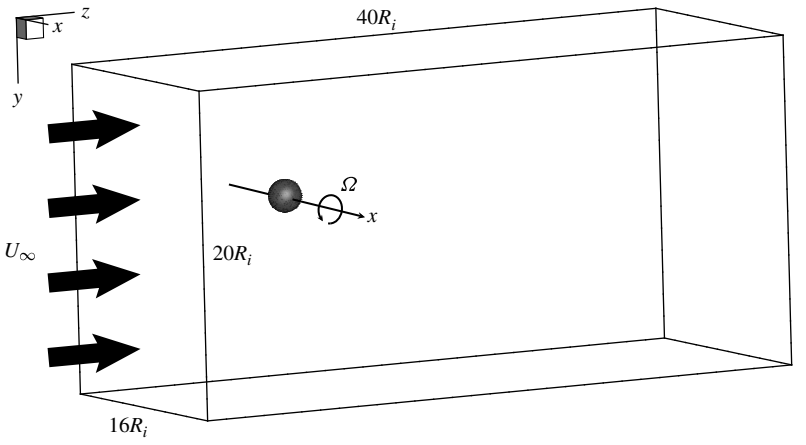


FIGURE 1. A representation of the computational domain. A droplet initially rotates in the x-direction with angular velocity Ω. A uniform crossflow in the z-direction accelerates the droplet impulsively.

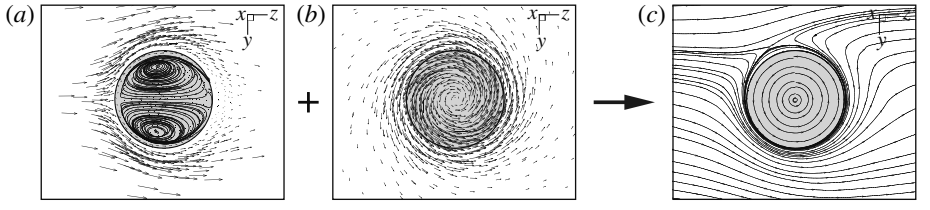


FIGURE 2. The velocity distribution (in the yz-plane): (a) a uniform flow, U_∞, past a spherical droplet, (b) a transversely rotating spherical droplet and (c) the superimposed velocity field of a uniform flow past a transversely rotating spherical droplet. The droplet is represented by a grey circle and the interface is represented by a black line.

free stream, U_∞, in the z-direction. The computational domain has a size of $40R_i$ in length (z-direction), $20R_i$ in height (y-direction) and $16R_i$ in depth (x-direction). The droplet is initially located at the origin $(x, y, z) = (0, 0, 0)$ of the Cartesian coordinate system, which is $10R_i$ from the inlet, $5R_i$ from the top wall and $8R_i$ from either of the sidewalls. At the inlet, a uniform free-stream velocity, U_∞, is imposed. The four sidewalls are prescribed to be U_∞. An outflow boundary condition is applied at the downstream face of the computation domain. The droplet is free to deform and travel downstream.

The initial flow field as shown in figure 2(c) is obtained by superimposing the steady-state velocity fields of a uniform flow past a spherical droplet (see figure 2a) and a spherical droplet rotating in the x-axis (see figure 2b). The details of setting up the uniform flow can be found in Quan & Schmidt (2006). A similar procedure is used for obtaining the steady-state rotating flow. The only difference is that a solid-body rotation velocity field is set for the droplet phase while the suspending fluid is stationary. Figure 3 shows the calculated steady-state velocity distribution for a rotating droplet together with the Stokes solution and the Rankine vortex for comparison. $r^* = r/R_i$ is the dimensionless position vector in the radial direction, $|U_C{}^*| = |U_C|/(R_i\Omega)$ represents the magnitude of the dimensionless cell-centre velocity

https://doi.org/10.1017/jfm.2011.298 Published online by Cambridge University Press

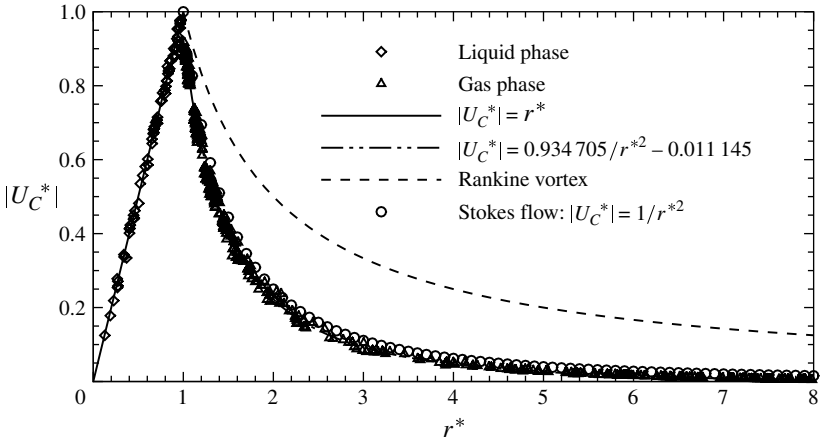


FIGURE 3. Initial velocity profiles in the radial (r) direction.

and $|U_C| = ({U_{Cx}}^2 + {U_{Cy}}^2 + {U_{Cz}}^2)^{1/2}$. The velocity inside the droplet ($r^* \leqslant 1$) represents the solid-body rotation, and the velocity in the matrix fluid closely approximates the Stokes result while it diverges from the Rankine vortex solution. The possible reason for the difference in velocity distribution is that the Rankine vortex is a solution of a two-dimensional inviscid flow, while we are solving a three-dimensional flow with finite viscosity. In the following simulation, different rotation rates can be achieved by varying the circulation of the droplet in figure 2(*b*).

The simulations in the current study are performed at an initial Reynolds number,

$$Re_i = \frac{\rho_m U_\infty 2R_i}{\mu_m} = 40, \tag{3.1}$$

where ρ is the density, μ is the dynamic viscosity, and the subscript m indicates the matrix. The droplet instantaneous Reynolds number is defined by

$$Re = \frac{\rho_m (U_\infty - U_{d,z}) 2R_i}{\mu_m}, \tag{3.2}$$

and $U_{d,z}$ is the droplet centroid velocity in the z-direction, calculated by a volume weighted average method,

$$U_{d,z} = \frac{\sum\limits_{cells} U_{C,z} V_C}{\sum\limits_{cells} V_C}, \tag{3.3}$$

where $U_{C,z}$ and V_C are the streamwise velocity of a cell and the volume of a cell, respectively. The initial Weber numbers are chosen as

$$We_i = \frac{\rho_m (U_\infty)^2 2R_i}{\sigma} = 0.4,\ 4 \text{ and } 40, \tag{3.4}$$

where σ represents the surface tension coefficient. The dimensionless rotation rates are

$$\Omega^* = \frac{\Omega R_i}{U_\infty} \in [0,\ 1]. \tag{3.5}$$

https://doi.org/10.1017/jfm.2011.298 Published online by Cambridge University Press

These Reynolds and Weber numbers are often found in applications such as inkjet printing and sprays (Son *et al.* 2008; Lubarsky *et al.* 2010). In this study, Ω^* is limited to unity in order to avoid droplet breakup at higher rotation rate, as observed by Bohr & Wheeler (1939) and Cardoso & Gualtieri (2006).

The trajectory of the unsteady motion of the droplet is controlled by the total hydrodynamics forces acting on it. As the movement of the interface is computed using the local interface velocity (in a Lagrangian manner) as mentioned in § 2.2, the advancement of the droplet centroid is a direct consequence of the interface movement. Using Newton's second law, the motion of the droplet centroid in the streamwise direction can be written in a similar way to that of Temkin & Kim (1980), Quan & Schmidt (2006) and Loth & Dorgan (2009), as

$$\frac{4}{3}\pi {R_i}^3 \rho_d \frac{\mathrm{d}U_{d,z}}{\mathrm{d}t} = \frac{1}{2}\pi {R_i}^2 \rho_m (U_\infty - U_{d,z})^2 C_D, \tag{3.6}$$

where ρ_d stands for the density of the droplet and C_D is the total drag coefficient. By employing (3.6), the contributions of the added mass, Basset history forces and the viscous forces are taken into account in C_D. It should also be noted that the initial droplet radius R_i is used in (3.6), as the droplet deformation is only known *a posteriori*. The total drag coefficient can be obtained by rearranging the equation of motion (3.6), and is given as

$$C_D = \frac{8R_i\eta}{3(U_\infty - U_{d,z})^2}\frac{\mathrm{d}U_{d,z}}{\mathrm{d}t}, \tag{3.7}$$

where $\eta = \rho_d/\rho_m$ is the density ratio. Likewise, the droplet's equation of motion in the lift (y-) direction is

$$\frac{4}{3}\pi {R_i}^3 \rho_d \frac{\mathrm{d}U_{d,y}}{\mathrm{d}t} = \frac{1}{2}\pi {R_i}^2 \rho_m (U_\infty - U_{d,z})^2 C_L, \tag{3.8}$$

and the total lift coefficient, C_L, is

$$C_L = \frac{8R_i\eta}{3(U_\infty - U_{d,z})^2}\frac{\mathrm{d}U_{d,y}}{\mathrm{d}t}, \tag{3.9}$$

where $U_{d,y}$ is the y-component of the droplet centroid velocity.

In this study, the droplet undergoes large deformation and the surface and projected area of the droplet vary at any instant in time. The instantaneous frontal area non-dimensionalised by the projected area of the initially spherical droplet is given by

$$A^* = \frac{0.5\Sigma|\boldsymbol{n}_f \cdot \boldsymbol{z}|}{\pi R^2}, \tag{3.10}$$

where $\boldsymbol{n}_f$ and $\boldsymbol{z}$ are the face normal area and the unit vector in the z-direction, respectively. To take into account the droplet deformation effects on the drag and lift coefficients, we also define drag and lift coefficients based on the instantaneous frontal area as

$${C_D}^* = \frac{C_D}{A^*} \quad \text{and} \quad {C_L}^* = \frac{C_L}{A^*}. \tag{3.11}$$

3.2. *Mesh dependence*

The mesh dependence is studied by simulating a case with two different meshes: one with 100 000 elements and the other one with 200 000 elements. In both cases, the

https://doi.org/10.1017/jfm.2011.298 Published online by Cambridge University Press

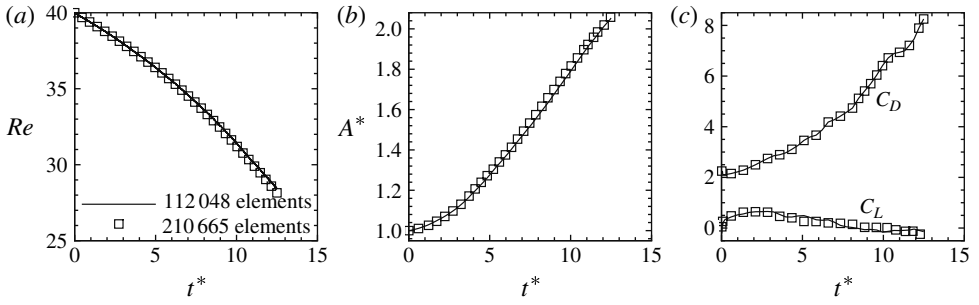


FIGURE 4. Study of mesh dependence for a rotating droplet at an initial Reynolds number, $Re_i = 40$, Weber number, $We_i = 40$ and non-dimensional rotation rate, $\Omega^* = 0.1$. The density ratio and viscosity ratio are set at $\eta = \lambda = 50$: (*a*) Re; (*b*) non-dimensional frontal area, A^* and (*c*) time-histories for the total lift and drag coefficients.

points are clustered towards the interface. The instantaneous Reynolds number, frontal area and the total drag and lift coefficients using the two grids are presented in figure 4. The results are found to be consistent, which proves that the spatial resolution of the simulations are adequate even with 100 000 elements in the computational grid. However, the grid with 200 000 elements is used for all calculations in the present study.

3.3. *Validation*

The numerical schemes have been analysed by Zhang, Schmidt & Perot (2002), and have been validated against a number of classical multiphase problems by Quan & Schmidt (2006, 2007) and Quan *et al.* (2009*a*,*b*).

To further validate the numerical methods, the dynamics of a deformable, rotating droplet is simulated. The initial flow field for the droplet is shown in figure 2(*b*). In this section, the rotation rate is normalised by Lamb's frequency (Lamb 1945) of the mode 2 oscillation (ω_2), instead of U_∞/R_i, in order to provide a direct comparison with data available in the literature. The non-dimensional rotation rate $\Omega/\omega_2 \in [0.2, 0.5]$, the density ratio $\eta = 20$, and the viscosity ratio $\lambda = 20$ are considered. Figure 5(*a*) presents the oscillation amplitude and the period of the initially rotating droplet. The width of the droplet, a, along the rotation (x-) axis is calculated by measuring the interface position, and it is non-dimensionalised by the initial droplet radius, R_i. As the droplet rotates, it is initially flattened at the poles by the induced centrifugal force. The deformation eases as the centrifugal force is balanced by the growing interfacial tension. As the surface tension increases to recover the spherical shape of the droplet, the droplet expands along the rotation axis and leads to an overshoot of a/R_i. The restoration of the droplet to a more spherical shape also increases the centrifugal force acting on the droplet, and the droplet contracts along the rotation axis again. This process repeats until the droplet loses all its kinetic and surface energy. Figure 5(*b*) displays the relative shift in frequency, $\Delta\omega/\omega_2$, together with analytical predictions (Busse 1984) and recent numerical solutions (Watanabe 2008). It should be noted that Watanabe's simulations were carried out at $Re_r = \rho_m \Omega R_i^2/\mu_m = 200$, while our simulations are performed at a maximum rotation Reynolds number of $Re_r = 40$. The present data at $\Omega/\omega_2 = 0.5$ is found to be consistent with the numerical solutions by Watanabe (2008), but the current results diverge away from the analytical solutions with decreasing Ω/ω_2. This

https://doi.org/10.1017/jfm.2011.298 Published online by Cambridge University Press

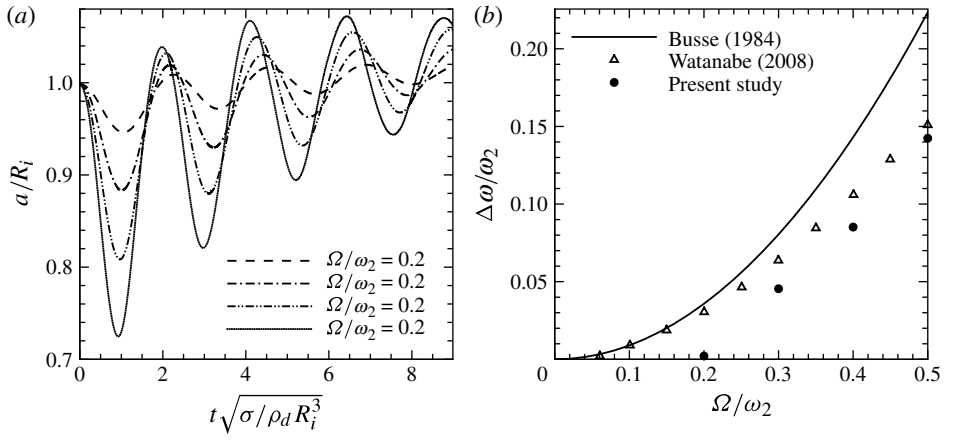


FIGURE 5. (*a*) Time-histories of the droplet oscillations due to an impulsive angular acceleration and (*b*) the corresponding frequency shift for each Ω/ω_2 together with data in the literature.

discrepancy may be attributed to the assumption of inviscid flow in the analytical solutions of Busse (1984). Our simulations do not have this restricted assumption.

4. Results and discussion

The results of a deformable, transversely rotating droplet suddenly accelerated by a uniform flow are presented. The droplet has an initial Reynolds number, $Re_i = 40$, and initial dimensionless rotational rates, $0 \leqslant \Omega^* \leqslant 1$, are considered. The effects of rotation on the deformation and dynamics of the droplet are investigated. The effects of viscosity ratio λ, density ratio η and initial Weber numbers We_i are also systematically studied.

4.1. *Effects of initial droplet rotation*

4.1.1. *Droplet topology at small Ω^**

In this section, the instantaneous droplet topology for $Re_i = We_i = 40$, $\eta = \lambda = 50$ is presented and will serve as the baseline case for this study. Figure 6 presents the instantaneous shape of the transversely rotating droplet for $\Omega^* \leqslant 0.2$. Each snapshot is taken at a non-dimensional time interval of $t^* = 2.5$, where $t^* = tU_\infty/R_i$. The evolution of a non-rotating droplet (i.e. $\Omega^* = 0$) is also presented as a reference for comparison. Under the influence of a uniform crossflow, the droplet is compressed by the free-stream inertia. The droplet deforms into an oblate spheroid in the early stages of the droplet evolution, with both the upwind and lee side of the droplet being continuously flattened. In the later stages of the simulation, the upwind side of the droplet becomes more obtuse while the lee side flattens. The droplet remains axisymmetric in the azimuthal direction throughout the entire simulation.

At $\Omega^* = 0.1$, the deformation sequence is similar to the non-rotating droplet (see results for $\Omega^* = 0.0$). As the droplet travels downstream it is tilted in the same direction as the droplet rotation. The transversely rotating droplet is also drawn downward (in the positive y-direction). In addition, the rotation has destroyed the axisymmetric property of the droplet. However, a symmetry plane perpendicular to the rotation axis (i.e. yz-plane) is observed for all Ω^* considered in the present study. The similarity of the behaviour of a deformable, transversely rotating droplet at small Ω^*

https://doi.org/10.1017/jfm.2011.298 Published online by Cambridge University Press

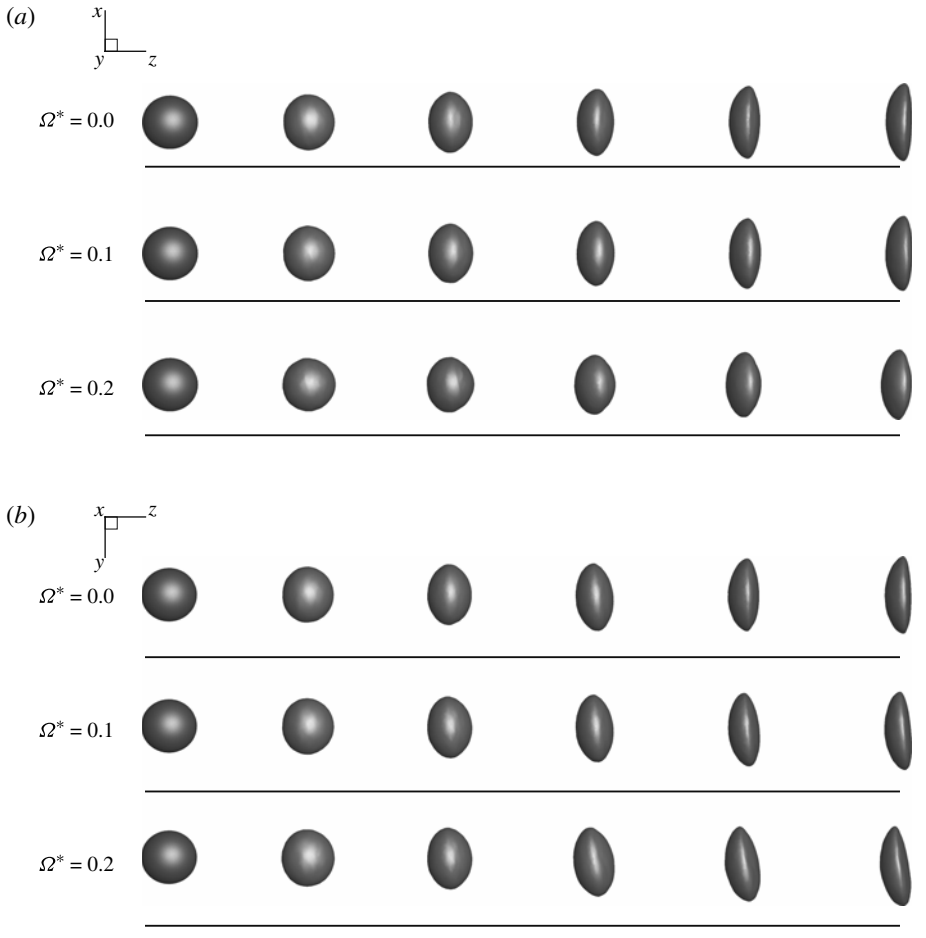


FIGURE 6. Instantaneous droplet shape for $Re_i = 40$, $We_i = 40$, $\eta = \lambda = 50$ and $\Omega^* \leqslant 0.2$. The snapshots are shown at dimensionless time t^*, from left to right, of 0, 2.5, 5, 7.5, 10 and 12.5: (*a*) (x, z)-plane and (*b*) (y, z)-plane.

to that of a non-rotating droplet in a free stream can be attributed to the rapid suppression of the rotation effect by the free stream. Although the droplet deformation sequence is similar, the rotation field generated by the initial conditions increases the local interface velocity at the bottom. As a result, the droplet is tilted and is vectored downward.

The effect of initial rotation on droplet shape evolution becomes more pronounced with increasing Ω^*. At $\Omega^* = 0.2$, although the droplet shape appears to be similar to that at $\Omega^* = 0.1$ in the early stages of evolution, the droplet is tilted at a larger angle as it evolves downstream (see figure 6*b*). The larger Ω^* causes a greater elongation of the droplet in the y-direction, while the expansion in the x-direction (see figure 6*a*) is reduced as compared to $\Omega^* = 0.1$. Furthermore, there is a noticeable change in interface curvature (when viewed in the yz-plane) at the lowermost point of the droplet (maximum positive y-direction; see figure 6*b*) and the uppermost point of the droplet for $t^* > 7.5$. To examine the underlying physics of the effects of transverse rotation, time sequences of the streamlines and velocity vectors in a reference frame moving

https://doi.org/10.1017/jfm.2011.298 Published online by Cambridge University Press

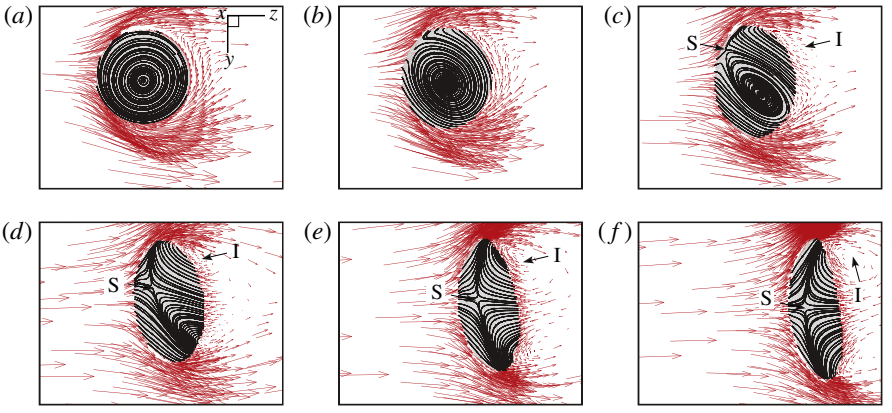


FIGURE 7. Evolution of velocity field inside the droplet with $Re_i = 40$, $We_i = 40$, $\Omega^* = 0.2$ and $\eta = \lambda = 50$: (*a*) $t^* = 0$, (*b*) $t^* = 2.5$, (*c*) $t^* = 5$, (*d*) $t^* = 7.5$, (*e*) $t^* = 10$, and (*f*) $t^* = 12.5$. The shaded region represents the droplet cross-section area on the (y, z)-plane. I is the induced vortex; S is the saddle.

with the droplet centroid are shown in figure 7. At $t^* = 0$, a circular vortex exists inside the droplet. The presence of the free stream deforms and tilts the vortex anticlockwise (figure 7*b*,*c*), which results in the tilting of the droplet. The deformed vortex continues to tilt while the tilting of the droplet is restrained by the formation of the induced vortex I, as shown in figure 7(*c*). At the same time, a saddle (S; Chong, Perry & Cantwell 1990) is formed at the upper leading edge of the droplet. As the droplet evolves, the saddle S is pushed to the centre of the droplet while the central vortex is pushed to the bottom lee side of the droplet. It is the reverse flow of this vortex that induces another recirculation region I, as seen in figure 7(*c–f*). Unlike a non-rotating droplet, there is a difference in size between the two recirculations for the transversely rotating droplet. The induced vortex results in an increase in fluid velocity (on the upper lee side interface) in the negative y-direction. As a result, the velocity of the upper saddle is increased and the droplet flattens and elongates in both positive and negative y-directions. It should be noted that because the interface changes its shape with time, the streamlines are shown to cross the interface. However, as the interface moves in a Lagrangian fashion, the two fluids do not mix.

The changing flow field past the droplet has also affected the localised curvature at the lowermost and uppermost points of the interface. Figure 8(*a*) presents the velocity contour and streamlines in a stationary reference frame. The colour contour shows that the velocity at the uppermost point of the interface is slightly higher than the velocity at the lowermost point of the interface. In order to explain these features, the streamlines are plotted in a reference frame moving with the droplet centroid in figure 8(*b*). At this time instant, an induced vortex (as marked in figure 8*b*) has formed. The induced vortex vectors the streamlines near the uppermost interface in the direction of the free stream and accelerates the flow there. The increase in local velocity at the uppermost interface leads to a local Weber number, $We_l = \rho_d U_l^2 2R_i/\sigma = 0.3805$, where the local Weber number indicates the ratio of the free-stream momentum to the surface tension of the interface, subscript d represents the droplet and U_l is the localised interface velocity. On the other hand, near the lowermost point of the interface, the streamlines are pointing downward but not in the free-stream direction. As a result, the local velocity at the lowermost interface point

https://doi.org/10.1017/jfm.2011.298 Published online by Cambridge University Press

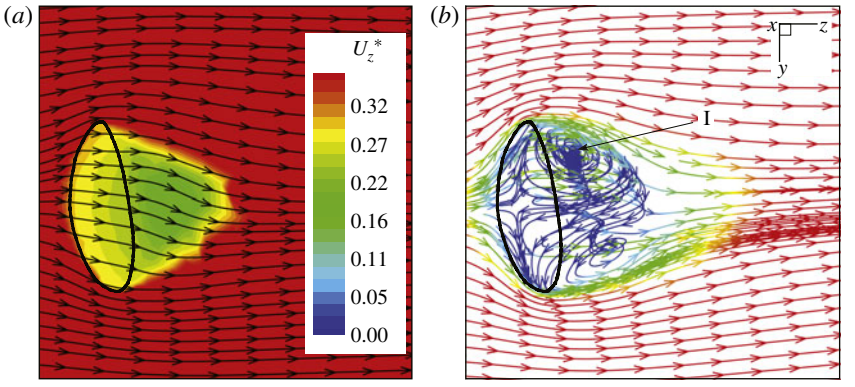


FIGURE 8. Instantaneous projected streamlines onto the (y, z)-plane for initial $Re_i = 40$, $We_i = 40$, $\Omega^* = 0.2$ and $\eta = \lambda = 50$ at $t^* = 12.5$: (*a*) stationary reference frame and (*b*) reference frame moving with the droplet centroid. The solid line displays the instantaneous droplet shape. I is the induced vortex.

is not as high as at the uppermost interface point and a lower local Weber number of $We_l = 0.1545$ is calculated. The difference in local Weber numbers allows the droplet to deform differently. The deformation is more pronounced with a higher local Weber number and is inhibited for smaller local Weber number. Also evident in figure 8(*a*) are the deflected streamlines in the near wake. The deflected streamline is a result of the formation of the induced vortex, I (see figure 8*b*), which draws fluids in the near wake downward as seen in figure 8(*a*). And by the conservation of momentum, we deduce that the droplet is experiencing a negative lift coefficient. The time-history lift coefficient will be discussed in § 4.1.3.

4.1.2. *Droplet topology at large* Ω^*

Figure 9(*a*) presents the droplet evolution for $\Omega^* \geqslant 0.4$. At $\Omega^* = 0.4$, there is a notable change in droplet evolution at earlier times. The compression of the droplet along the rotation axis becomes more obvious; this flattening of the droplet is also linked to the radial expansion of the droplet normal to its rotation axis. As expansion of the droplet normal to the rotation axis slows down and the droplet becomes tilted in a similar fashion to those observed for $\Omega^* \leqslant 0.2$. It is also evident in figure 9(*b*) that a small depression appears on the side of the droplet. In order to understand the physics that governs the change in droplet evolution, the droplet rotation Weber number, $We_r = 2\rho_m(\Omega R_i)^2 R_i/\sigma$, is considered. We_r indicates the relative strength of the centrifugal force to the interfacial surface tension. It is found that at $\Omega^* = 0.1$ and 0.2, $We_r = O(0.1)$ and $O(1)$, respectively. This indicates that the centrifugal force is not sufficient to overcome the interfacial surface tension. In addition, although the centrifugal force results in small compression of the droplet along the rotation axis, it is quickly overshadowed by the free-stream momentum as $We_r = O(1)$ or less. However, at $\Omega^* = 0.4$, $We_r = O(10)$ and the centrifugal force is large enough to overcome the surface tension. As the droplet expands radially, the tangential interface velocity reduces in order to conserve angular momentum. This reduction in tangential velocity may also be attributed to the transfer of rotational kinetic energy from the droplet to the surface energy at the interface. As the rotational kinetic energy diminishes, the droplet stops expanding and the free-stream effect dominates and compresses the upwind side of the droplet, which leads to the occurrence of the small

https://doi.org/10.1017/jfm.2011.298 Published online by Cambridge University Press

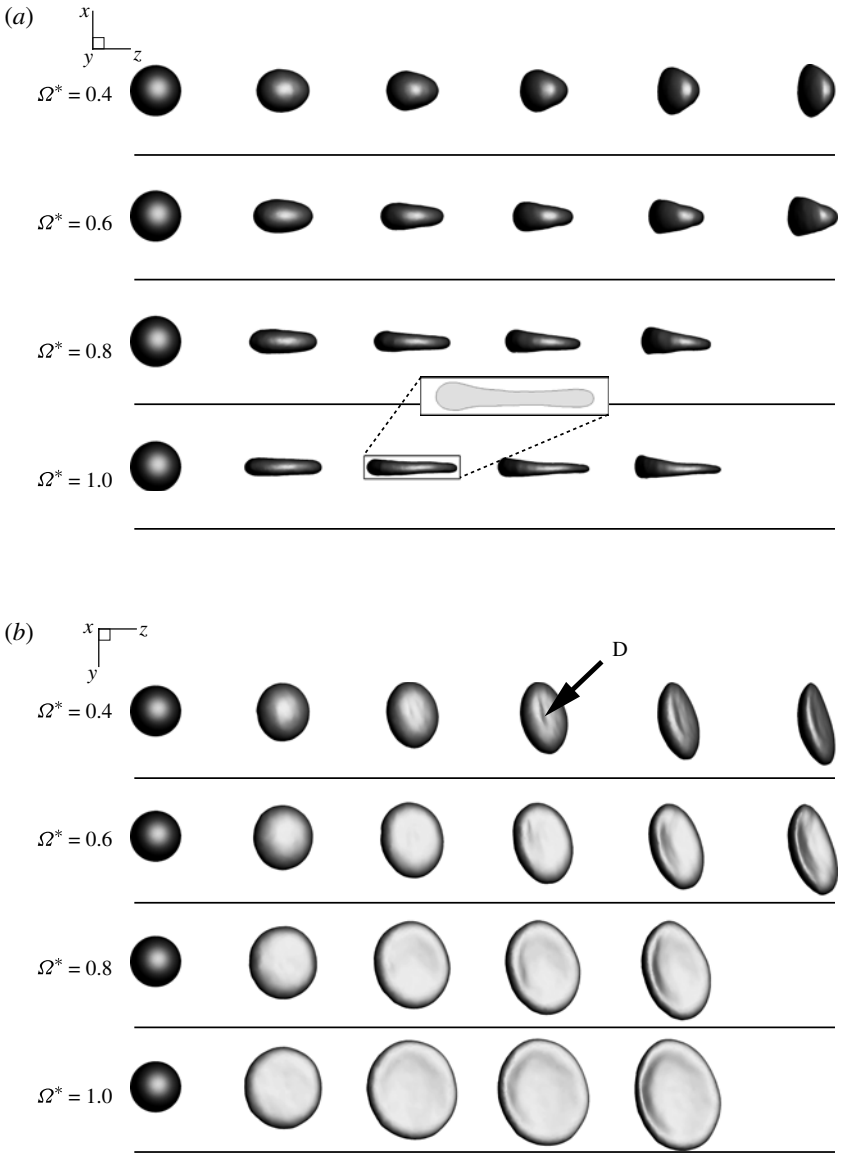


FIGURE 9. Instantaneous droplet shape for $Re_i = 40$, $We_i = 40$, $\eta = \lambda = 50$ and $\Omega^* \geqslant 0.4$. The snapshots are shown at dimensionless time t^*, from left to right, of 0, 2.5, 5, 7.5, 10 and 12.5: (*a*) (x, z)-plane and (*b*) (y, z)-plane. D is the depression of the interface due to the combined effect of free stream and rotation.

depression, D. Although a droplet depression is often found for a rotating droplet in a stationary matrix at large rotation rate (Chandrasekhar 1965; Brown & Scriven 1980; Cardoso & Gualtieri 2006), the mechanism responsible for the depression at $\Omega^* = 0.4$ is different from those mentioned in previous studies. The depression found here becomes visible when the free stream begins to dominate. The dominating free stream creates a flat upwind interface whereas the history effect of the droplet rotation compresses the lee side of the droplet along the rotation axis, creating a depression as shown in figure 9(*b*). The occurrence of the depression at $\Omega^* = 0.4$ can therefore be

https://doi.org/10.1017/jfm.2011.298 Published online by Cambridge University Press

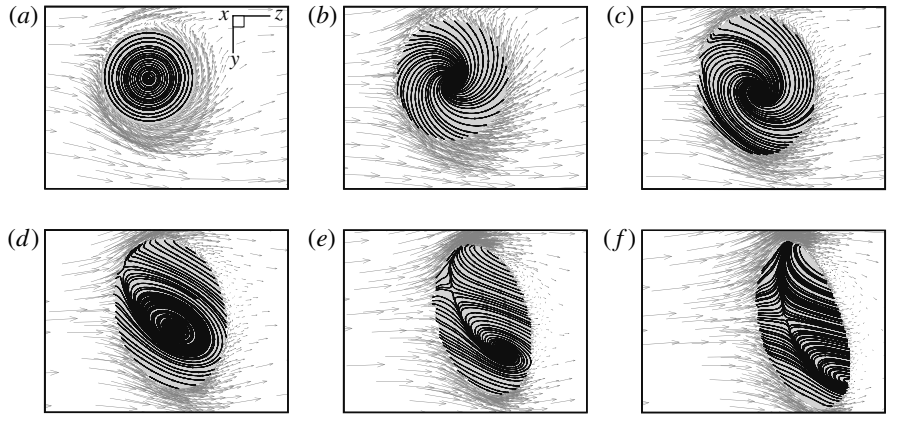


FIGURE 10. Evolution of velocity field inside an initially rotating droplet at $Re_i = 40$, $We_i = 40$, $\Omega^* = 0.6$ and $\eta = \lambda = 50$: (*a*) $t^* = 0$, (*b*) $t^* = 2.5$, (*c*) $t^* = 5$, (*d*) $t^* = 7.5$, (*e*) $t^* = 10$ and (*f*) $t^* = 12.5$. The shaded region represents the droplet cross-section area on the (y, z)-plane.

attributed to the combination of both free-stream and rotation effects. The difference in droplet deformation evolution at $\Omega^* = 0.4$ as compared to $\Omega^* = 0.2$ indicates that the droplet deformation sequence has undergone a distinct change in between these Ω^*s. Herein, we refer to the dimensionless rotation rate where the droplet deformation changes substantially as the ${\Omega_{crit}}^*$, where the free-stream effect dominates below the ${\Omega_{crit}}^*$ and the rotation effect dominates above the ${\Omega_{crit}}^*$.

The evolution of the droplet at $\Omega^* = 0.6$ shows a similar trend to $\Omega^* = 0.4$, except that the droplet is spun further away from the rotation axis due to the higher rotational velocity. As the droplet is spun further away from the rotation axis, the surface tension at its edge increases and prevents further deformation at its edge and the droplet takes a biconcave shape. Since the depression appears while the centrifugal force is still expanding the droplet, this depression arises mainly due to the droplet rotation instead of the presence of free-stream momentum. The tilting of the droplet is also delayed due to the stronger rotation, which keeps the droplet expanding for a longer period. In order to confirm that the increase in Ω^* has led to a delay in droplet tilting, the streamlines in a moving reference frame for $\Omega^* = 0.6$ are plotted in figure 10. At $\Omega^* = 0.6$, droplet deformation is dominated by rotation effects due to a large rotation Weber number, $We_r = O(10)$. The radially outward expansion of the droplet helps to hold the unstable focus structure at the droplet centroid, as seen in figure 10(*b*,*c*) for a longer period. In addition, the unstable focus structure maintains its shape for a longer time and is only tilted and deformed after the droplet stops contracting at its poles (see figure 10*d*). The tilting and deformation of the vortex inside the droplet are the primary mechanisms responsible for the tilting of the droplet, and these mechanisms are delayed at $\Omega^* = 0.6$.

A further increase of Ω^* to 0.8 and 1 increases the centrifugal force such that the droplet becomes biconcave in shape (see inset in figure 9*a*) at earlier stages (at $t^* \leqslant 5$) compared to $\Omega^* < 0.8$. For $\Omega^* \geqslant 0.8$, the droplet becomes extremely thin and the number of grid points required for a smooth interface at the edge of the droplet increases dramatically. Therefore, simulations were stopped before $t^* = 12.5$ to minimise computational cost, since the effects of rotation have already diminished for $t^* > 10$.

https://doi.org/10.1017/jfm.2011.298 Published online by Cambridge University Press

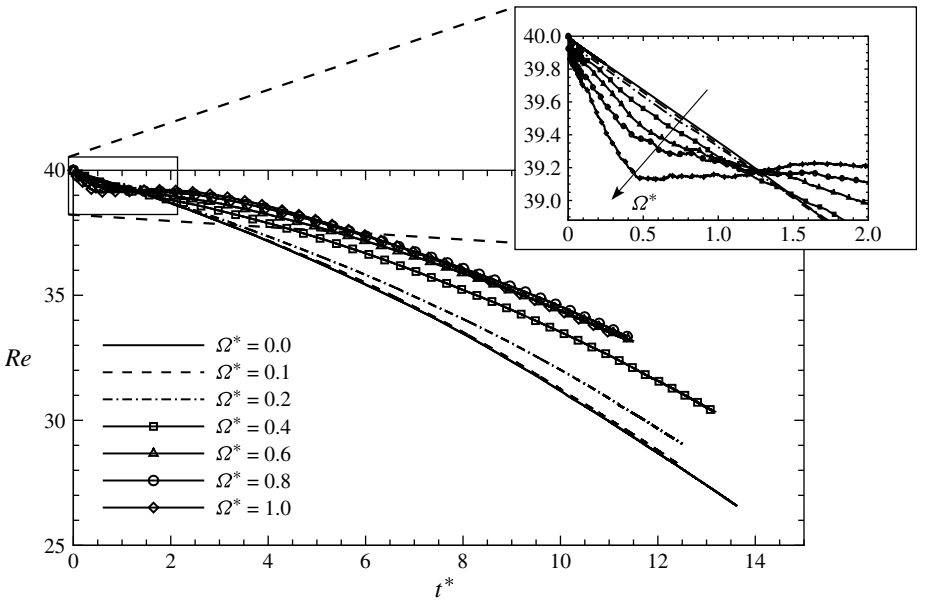


FIGURE 11. Instantaneous Reynolds number Re for the droplet at $Re_i = 40$, $We_i = 40$, $\eta = \lambda = 50$ and $0 \leqslant \Omega^* \leqslant 1$.

4.1.3. *Instantaneous Reynolds numbers, force coefficients and frontal areas*

Figure 11 displays the time-histories for the instantaneous Reynolds number of the droplet. The instantaneous Reynolds number represents the non-dimensionalised droplet velocity in the streamwise direction. For $\Omega^* \leqslant 0.2$, the time-history of Re is very similar to that of a non-rotating droplet. With increasing Ω^*, Re decreases sharply for $t^* < 0.5$ (see inset of figure 11). For $0.5 \leqslant t^* \leqslant 1.3$, the decrease in Re is more gradual for large Ω^*. Beyond $t^* \approx 1.3$, there is a cross-over point with Re showing a slower decrease with increasing Ω^*. The major reason for the sharper decrease in Re (at earlier stages of the flow) for large Ω^* can be attributed to the relatively higher velocity on the lee side of the droplet as compared to the upwind side. The Re behaviour for $t^* \geqslant 1.3$ is attributed to the droplet deformation and will be discussed with the aid of the non-dimensionalised frontal area, A^*.

The instantaneous frontal area is presented in figure 12. As discussed in §§ 4.1.1 and 4.1.2, there exists a $\Omega_{crit}{}^*$ which divides the droplet deformation into two regimes. These regimes can be easily distinguished in figure 12. For $\Omega^* \leqslant 0.2$, the droplet deformation is free-stream-dominated and A^* rises monotonically with time. The slower increase in A^* initially for $\Omega^* = 0.1$ and 0.2 is a result of the droplet being slightly compressed at its pole by the transverse rotation. The effect of rotation diminishes quickly and is suppressed by the free-stream momentum, which leads to a steadily increasing A^*. For $\Omega^* \geqslant 0.4$, two different modes of deformation are at play: it is initially flattened by the rotation at its pole and later flattened by the free-stream momentum. When the droplet is flattened by the large centrifugal force at its pole for $\Omega^* \geqslant 0.4$, A^* decreases substantially. The difference in A^* becomes less when Ω^* approaches 1 as the sharp curvature at the interface prevents further deformation (see cases with $\Omega^* = 0.6$, 0.8 and 1). Once the rotation effect diminishes, the free-stream momentum dominates and A^* increases at a similar rate for all cases considered.

https://doi.org/10.1017/jfm.2011.298 Published online by Cambridge University Press

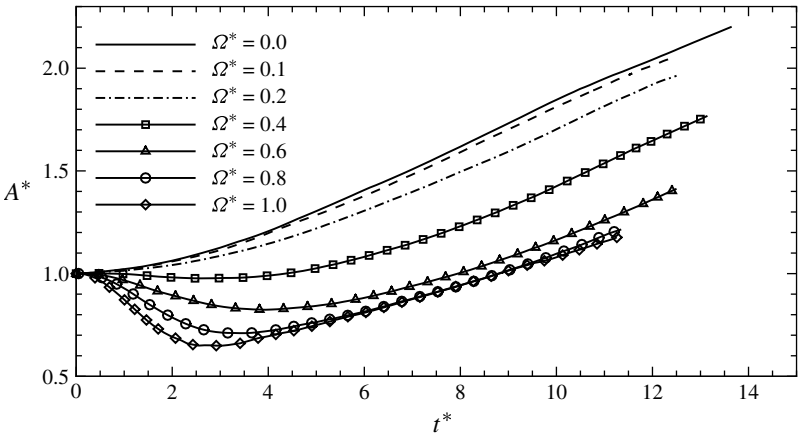


FIGURE 12. Instantaneous frontal area A^* for the droplet at $Re_i = 40$, $We_i = 40$, $\eta = \lambda = 50$ and $0 \leqslant \Omega^* \leqslant 1$.

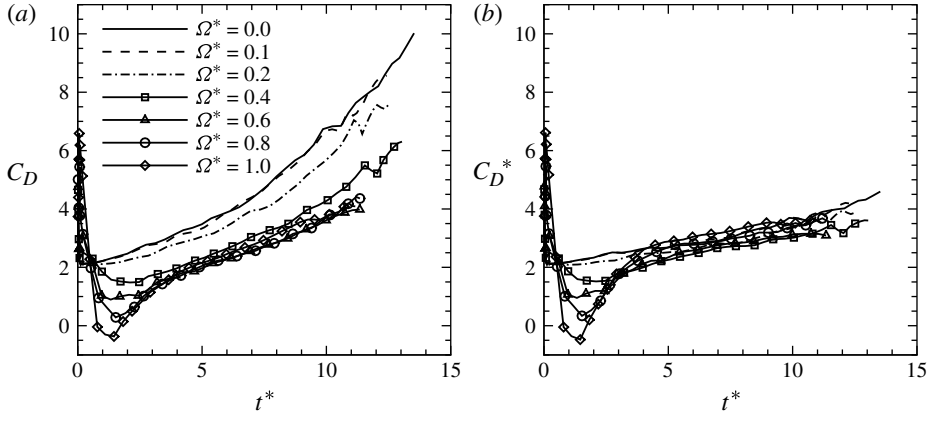


FIGURE 13. Drag coefficient histories for the droplet at $Re_i = 40$, $We_i = 40$, $\eta = \lambda = 50$ and $0 \leqslant \Omega^* \leqslant 1$: (*a*) total drag coefficient based on the initial spherical droplet frontal area C_D, and (*b*) drag coefficient based on the changing droplet frontal area $C_D{}^*$.

Figure 13(*a*) presents the total drag coefficient histories based on the initial spherical frontal area (3.7). The total drag coefficient, C_D, represents the combined effect of the droplet acceleration and the changing frontal area. For $\Omega^* \leqslant 0.2$, C_D follows a similar trend to a non-rotating droplet. The decreases in A^* lead to a lower C_D as Ω^* increases. For $\Omega^* \geqslant 0.4$, C_D shows a global minimum in the early stages. The minimum decreases with increasing Ω^*. However, in the later stages of its evolution, C_D increases steadily as the droplet rotation is suppressed by the free-stream momentum. To further analyse the frontal area effect on the drag, histories of the drag coefficients based on the changing frontal area, $C_D{}^*$, are plotted in figure 13(*b*). It is clearly observed that when Ω^* is small, $C_D{}^*$ collapses onto the same curve as a non-rotating droplet. This indicates that the effect of the free stream dominates for $\Omega^* \leqslant 0.2$. In contrast, when Ω^* increases to above 0.4, similar global minima are observed at earlier time as in figure 13(*a*). It is also interesting to note that there

https://doi.org/10.1017/jfm.2011.298 Published online by Cambridge University Press

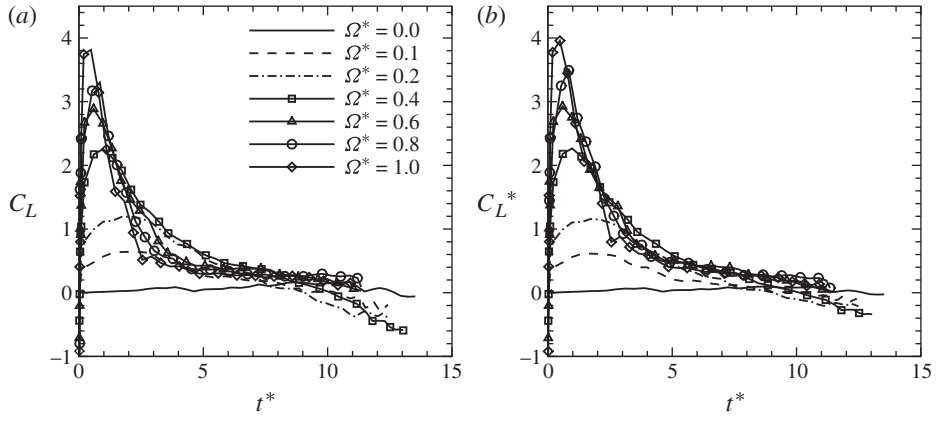


FIGURE 14. Lift coefficient histories for the droplet at $Re_i = 40$, $We_i = 40$, $\eta = \lambda = 50$ and $0 \leqslant \Omega^* \leqslant 1$: (*a*) total lift coefficient based on the initial spherical droplet frontal area C_L, and (*b*) lift coefficient based on the changing droplet frontal area $C_L{}^*$.

is only a slight difference between C_D and $C_D{}^*$ before $t^* \approx 1.5$, which suggests that the drag force acting on the droplet is substantially reduced by droplet rotation. The acceleration of the droplet for this period of time ($0.5 < t^* < 1.3$) and large Ω^* can be obtained from the slope of Re in the inset of figure 11. At later times, the centrifugal force diminishes and the droplet mainly experiences the free-stream momentum. As a result, $C_D{}^*$ tends toward those results observed for $\Omega^* \leqslant 0.2$. From the above analysis, it can be concluded that with sufficiently large Ω^*, the drag coefficients of the droplet can be reduced initially. However, once the transverse rotation comes to a halt, $C_D{}^*$ becomes similar to a non-rotating droplet.

Figure 14(*a*,*b*) shows the lift coefficient histories for the droplet based on the initial droplet frontal area, C_L, and the changing frontal area, $C_L{}^*$, respectively. It is observed that the difference between C_L and $C_L{}^*$ is less obvious across the range of Ω^* considered, as the vertical acceleration of the droplet is mainly due to the velocity difference between the upper and lower surface of the droplet. The initial rotation of the droplet in the positive x-direction leads to a positive lift coefficient in the y-direction for almost all cases. The only exception is that negative lift coefficients are observed for $\Omega^* = 0.1$, 0.2 and 0.4 at later times. In § 4.1.1, we attribute the negative lift force to the motion of the droplet centroid in the negative y-direction using a conservation of momentum argument, and link this motion to the formation of the induced vortex. It is also observed in both figures 14(*a*) and 14(*b*) that the absolute maximum lift coefficients occur at a earlier t^* with increasing Ω^* and the lift coefficients show a rapid decrease after reaching the maximum for $\Omega^* \geqslant 0.4$. The decrease is due to the continuous slowdown of the interfacial velocity as the droplet expands radially away from the rotation axis.

To further investigate the effects of droplet expansion on its interface velocity, the dimensionless tangential velocity ($u_t{}^*$) profile of the droplet through its centroid along the y-direction is shown in figure 15(*a*). As the droplet expands, the velocity profiles become less steep and the values at the interface decrease significantly, which leads to a decrease in C_L. To support this argument, the lift force exerted on the droplet is predicted using the Kutta–Joukowski theorem, $L \propto u_t R_{cyl}$, where u_t is the tangential velocity and R_{cyl} is the radius of the cylinder. For $t^* \leqslant 5$, the effect of

https://doi.org/10.1017/jfm.2011.298 Published online by Cambridge University Press

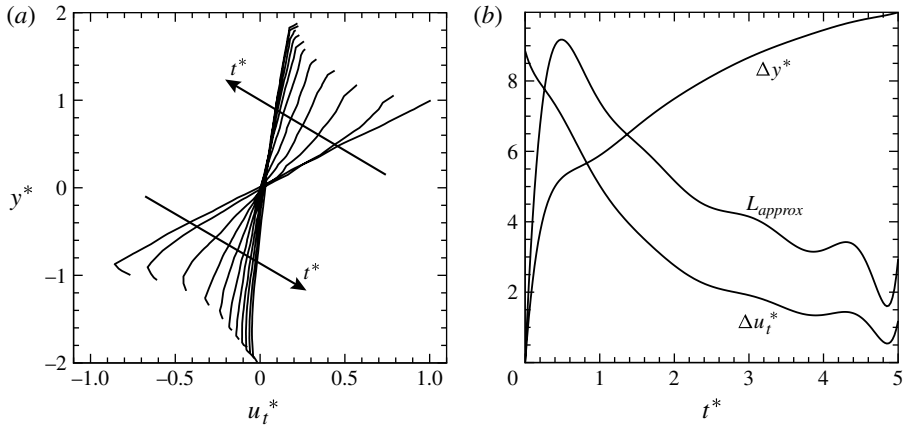


FIGURE 15. (*a*) Instantaneous velocity profile of the droplet in the *y*-direction through its centroid at $Re_i = 40$, $We_i = 40$, $\Omega^* = 1$ and $\lambda = \eta = 50$. (*b*) Difference in droplet velocity, Δu_t^*, interface position, Δy^*, between the highest and lowest y^* position, and the approximate lift force, L_{approx}, calculated using the Kutta–Joukowski lift theorem.

Case	We_i	λ	η	Ω^*	Objective
I	40	50	50	$\in [0, 1]$	The effects of Ω^*
II	40	100	50	0.2, 0.6, 1.0	The effects of droplet viscosity
III	40	50	10	0.2, 0.6, 1.0	The effects of droplet density
IV	4	50	50	0.2, 0.6, 1.0	Influence of interfacial surface tension
V	0.4	50	50	0.2, 0.6, 1.0	Influence of interfacial surface tension

TABLE 1. A summary of the parametric studies performed and the corresponding objective.

crossflow on the droplet is small and we can thus assume that the (y, z)-cut-plane of the droplet remains circular. If we also assume that the droplet angular velocity is constant on the interface, the lift force exerting on the droplet can be approximated as $L_{approx} \propto (\Delta u_t^* \Delta y^*)/4$. Figure 15(*b*) presents the evolution of L_{approx} together with Δu_t^* and Δy^*, where Δu_t^* and Δy^* are the differences in tangential interface velocity and interface position in the *y*-direction, respectively. It can be seen that the maximum L_{approx} occurs at approximately the same t^* as the peak in C_L. Further expansion of the droplet slows down the interface velocity and eventually leads to a decrease in L_{approx}, which is consistent with the trend of C_L. We can therefore conclude that the reduction in C_L in our simulations is due to further droplet expansion and reduction of the interface velocity. In addition, the faster the droplet expands, the steeper the C_L declines.

4.2. *Influence of viscosity ratio, density ratio and surface tension*

In this section, the influence of the viscosity ratio, density ratio and surface tension are studied in turn. Table 1 summarises the studies performed. Initial droplet deformations are found to be qualitatively similar even with different droplet properties, except for case III where the droplet density is reduced. Figure 16 presents a graphical representation of the regime where a change in droplet shape takes place for all cases considered. For cases I, II, IV and V, the droplet density is unchanged, and therefore

https://doi.org/10.1017/jfm.2011.298 Published online by Cambridge University Press

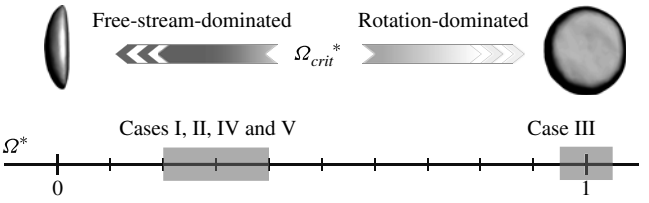


FIGURE 16. A graphical representation of the regime where a change in droplet shape takes place for all cases mentioned in table 1. To the left, the droplet is flattened by the free-stream momentum along the streamwise axis; to the right, the rotation effect dominates and the droplet is flattened along the rotation axis. The grey box along the line indicates the regime of Ω^* where the distinct change in droplet shape takes place.

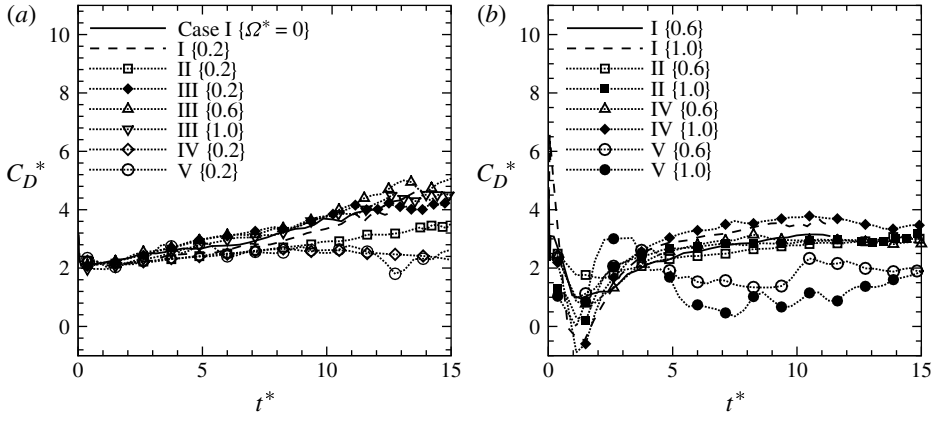


FIGURE 17. Time-histories of C_D^*: (*a*) dominating free-stream momentum and (*b*) dominating rotation effects.

the initial droplet angular momentum is the same initially for these cases. This implies that the centrifugal force acting on the droplet is the same. As a result, the initial deformation for the droplet is qualitatively similar and the Ω_{crit}^* is unchanged. The effects of increasing viscosity and surface tension only become obvious at later times and will be discussed later. However, for case III, the droplet density is decreased to lower the density ratio ($\eta = 10$). The angular momentum is thus reduced by 5 times and thus the droplet experiences a lower centrifugal force. The effect of free stream soon suppresses the effect of rotation for all Ω^*. But the droplet deformation starts to show signs of flattening for case III at $\Omega^* = 1$, similar to those observed for case I at $\Omega^* = 0.2$. This is because the decrease in droplet density leads to a proportional decrease in the centrifugal force. As a result, the Ω^* required to deform the droplet such that it deforms in a qualitatively similar fashion to those in case I has to be increased by the same factor. Although the Ω^* is limited to 1 in this study, it is expected that the Ω_{crit}^* where the initial droplet deformation changes significantly will occur slightly above 1 for case III.

Figure 17 presents the C_D^* for all the cases listed in table 1. It is evident that, aside from case III, all other cases settle into a regime similar to those observed for the baseline case I, i.e. C_D^* behaves differently between $\Omega^* = 0.2$ and 0.6. As previously mentioned, the change in droplet behaviour for case III to large Ω^* is due to the

https://doi.org/10.1017/jfm.2011.298 Published online by Cambridge University Press

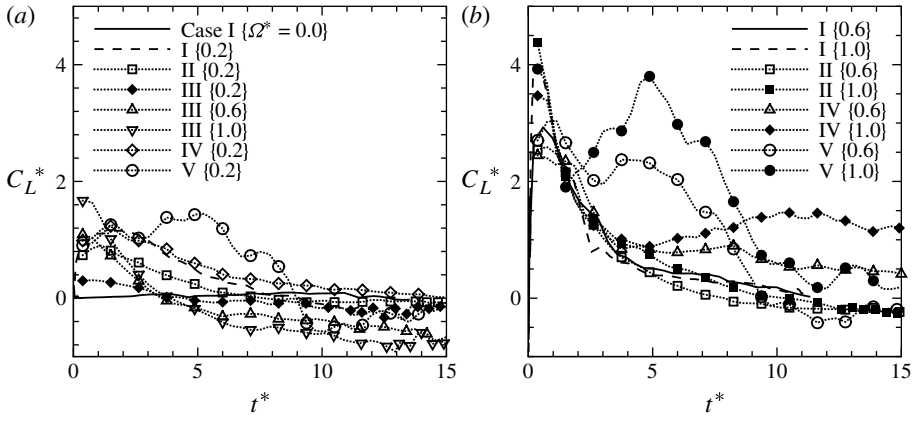


FIGURE 18. Time-histories of C_L^*: (*a*) dominating free-stream momentum and (*b*) dominating rotation effects.

substantial decrease in angular momentum. As a result, droplet deformations now fall into the free-stream-dominated regime as shown in figure 16 and C_D^* collapses with those for case I at $\Omega^* \leqslant 0.2$. For case II, even through the Ω_{crit}^* is within a range similar to that of case I, a slight difference in C_D^* at later times is observed in figure 17(*a*) and at earlier times in figure 17(*b*). The difference is due to the increase in droplet viscosity that inhibits droplet deformation (Quan & Schmidt 2006). As a result, a larger force is required to further deform the droplet. The influence of surface tension can also be seen in figure 17, where C_D^* is observed to diverge from all other cases at later times. As the droplet deforms, the surface tension at the sharp edges dramatically increases and restrains any further deformation of the droplet. As a result, the droplet frontal area is very different from case I. For the extreme We_i (case V), the droplet returns to a more spherical shape. Thus, the change in C_D^* reaches a minimum and its average value is roughly equal to those for a spherical droplet.

The time-histories of C_L^* are presented in figure 18. For case II, the increase in droplet viscosity leads to a more rapid energy dissipation and thus quickly slows down the droplet rotation. Therefore, C_L^* becomes smaller than those for case I. For case III, the droplet rotation is rapidly suppressed as the initial angular momentum is reduced. This also leads to a lower C_L^* as compared to case I at later times. For case IV and V, the surface tension increases significantly as the curvatures decreases, C_L^* is therefore only affected at later times. It is also worth mentioning that with increasing surface tension coefficient, σ, a second peak is observed for C_L^* for case V. This second peak is due to the increase in interface velocity as the droplet returns to a more spherical shape. The larger velocity difference between the upper and lower interface region leads to a greater pressure difference on the droplet along the y-direction and thus an increase in C_L^*. Although the magnitudes of C_L^* have been modified due to the change in droplet properties, we are still able to classify the results into the two specific groups as demonstrated in figure 16.

5. Conclusions

A transversely rotating droplet suddenly accelerated by a uniform free stream is numerically simulated to study the droplet deformation and dynamics. The effects of the transverse rotation on the droplet were first investigated at an initial Reynolds

https://doi.org/10.1017/jfm.2011.298 Published online by Cambridge University Press

number, $Re_i = 40$, an initial Weber number, $We_i = 40$, viscosity and density ratios, $\lambda = \eta = 50$. The initial dimensionless rotation rates are chosen to be in the range $0 \leqslant \Omega^* \leqslant 1$. It is found that the introduction of a transverse rotation on the droplet substantially modifies the droplet deformation. Depending on Ω^*, the droplet deformation can be classified into two regimes: free-stream-dominated and rotation-dominated. For $\Omega^* \leqslant 0.2$, the centrifugal force is relatively weak and is quickly suppressed by the free stream. Although droplet rotation is relatively weak, it slightly reduces the droplet frontal area and thus reduces the total drag coefficient based on the initial droplet frontal area C_D. The drag coefficient based on the dynamic droplet frontal area $C_D{}^*$ for all Ω^* considered collapses onto a single curve because of the dominating free-stream momentum. The transverse rotation also leads to droplet tilting as it is convected downstream. The tilting is a result of the vortex inside the droplet being deformed and tilted by the crossflow. In addition, the droplet is drawn and elongated towards the retreating side (velocity of the interface in the direction of the free stream) resulting in a positive lift coefficient. As the droplet evolves, a secondary vortex is formed across the upper lee side of the interface. This induced vortex elongates the droplet in the opposite direction and leads to a negative lift coefficient. The lift coefficient is less affected by the droplet frontal area as it mainly depends on the velocity difference between upper and lower droplet surface.

For $\Omega^* \geqslant 0.4$, the evolution of the droplet lies in the rotation-dominated regime and its deformation is distinctively different. The droplet is initially flattened at its poles, which leads to a dramatic decrease in frontal area and large reduction in both C_D and $C_D{}^*$ at earlier times. This large reduction in both C_D and $C_D{}^*$ results in a global minimum in the time-histories of coefficients which is not observed for low Ω^*. Once the rotation effects decrease, the free-stream effects dominate and $C_D{}^*$ for all Ω^* simulated collapses onto a single curve. The large Ω^* also sharply increases the lift coefficients acting on the droplet at early time. However, it is followed by a rapid decrease in lift coefficient after it reaches the peak value as the droplet expands radially outward. C_L is also found to decrease at a faster rate with increasing Ω^*. The radially outward expansion of the droplet works to keep the vortex inside the droplet for a longer period and thus delaying the effect of the crossflow inertia. Consequently, the lift coefficient remains positive throughout the simulation interval for large Ω^*.

The influence of the viscosity ratio, the density ratio and the surface tension on the droplet dynamics is also systematically studied. The critical dimensionless rotational rate, $\Omega_{crit}{}^*$, which divides the droplet deformations into the two different regimes are unaffected by the change in the viscosity ratios and the surface tension. But the $\Omega_{crit}{}^*$ is significantly increased by a decrease in density ratio, or specifically the increase in droplet density. This is because the initial angular momentum is directly proportional to the droplet density and a decrease in droplet density decreases the initial angular momentum. Since the droplet deformation can still be classified into free-stream-dominated or rotation-dominated regimes, $C_D{}^*$ and $C_L{}^*$ are qualitatively similar to the baseline case ($Re_i = 40$, $We_i = 40$, $\eta = \lambda = 50$ and $\Omega^* \in [0, 1]$). The difference only becomes obvious at later times when the increase in the droplet viscosity and the surface tension inhibits droplet deformation or restores the droplet to a more spherical shape.

The authors gratefully acknowledge support from the Agency for Science, Technology and Research (A*STAR), Singapore, through the A*STAR Research Attachment Programme (ARAP), and the Australian Research Council (Grant no.

https://doi.org/10.1017/jfm.2011.298 Published online by Cambridge University Press

DP0556098). We thank the referees for their valuable suggestions to improve the quality of our paper.

Appendix. Boundary conditions at the interface

In a sharp interface tracking method, the discontinuity in fluid properties across the zero-thickness interface are modelled by applying the following boundary conditions to Navier–Stokes equations. In the normal and tangential directions, the conservation of mass and linear momentum requires

$$(u_m)_n = (u_d)_n = u_n^{(mesh)}, \tag{A 1}$$

$$[\![u_t]\!] = 0, \tag{A 2}$$

$$[\![p]\!] = -\sigma\left(\frac{1}{K_m} + \frac{1}{K_d}\right) + [\![2\mu(\nabla \boldsymbol{u} \cdot \boldsymbol{n}) \cdot \boldsymbol{n}]\!], \tag{A 3}$$

$$\left[\!\!\left[\mu\left(\frac{\partial u_i}{\partial x_j} + \frac{\partial u_j}{\partial x_i}\right) t_i n_j\right]\!\!\right] = 0, \tag{A 4}$$

where p is the pressure, subscripts d, n and t represent droplet, normal and tangential components, respectively, K is the principal radius of the surface, and $[\![\ ]\!]$ denotes the difference across the interface. At the interface, the effective viscosity and the viscous shear are calculated using a geometric harmonic mean method (Quan & Schmidt 2007). The total curvature of the surface is predicted by a least-squares parabolic fitting method. The jump in viscous pressure, which is the last term in (A 3), is calculated using a first-order, multivariable Taylor series expansion.

REFERENCES

ANNAMALAI, P., TRINH, E. & WANG, T. G. 1985 Experimental study of the oscillations of a rotating drop. *J. Fluid Mech.* **158**, 317–327.

BISWAS, A., LEUNG, E. W. & TRINH, E. H. 1991 Rotation of ultrasonically levitated glycerol drops. *J. Acoust. Soc. Am.* **90**, 1502–1507.

BOHR, N. & WHEELER, J. A. 1939 The mechanism of nuclear fission. *Phys. Rev.* **56** (5), 426–450.

BROWN, R. A. & SCRIVEN, L. E. 1980 The shape and stability of rotating liquid drops. *Proc. R. Soc. Lond.* A **371**, 331–357.

BUSSE, F. H. 1984 Oscillations of a rotating liquid drop. *J. Fluid Mech.* **142**, 1–8.

CARDOSO, V. & GUALTIERI, L. 2006 Equilibrium configurations of fluids and their stability in higher dimensions. *Class. Quant. Grav.* **23** (24), 7151–7198.

CHABERT, M., DORFMAN, K. D. & VIOVY, J. L. 2005 Droplet fusion by alternating current (AC) field electrocoalescence in microchannels. *Electrophoresis* **26**, 3706–3715.

CHABREYRIE, R., VAINCHTEIN, D., CHANDRE, C., SINGH, P. & AUBRY, N. 2010 Using resonances for the control of chaotic mixing within a translating and rotating droplet. *Commun. Nonlinear Sci. Numer. Simul.* **15**, 2124–2132.

CHANDRASEKHAR, S. 1965 The stability of a rotating liquid drop. *Proc. R. Soc. Lond.* A **286**, 1–26.

CHANG, W., GIRALDO, F. & PEROT, B. 2002 Analysis of an exact fractional step method. *J. Comput. Phys.* **180**, 183–199.

CHONG, M. S., PERRY, A. E. & CANTWELL, B. J. 1990 A general classification of three-dimensional flow fields. *Phys. Fluids* A **2**, 765–777.

DAI, M. & SCHMIDT, D. P. 2005 Adaptive tetrahedral meshing in free-surface flow. *J. Comput. Phys.* **208**, 228–252.

DAI, M., WANG, H., PEROT, B. J. & SCHMIDT, D. P. 2002 Direct interface tracking of droplet deformation. *Atomiz. Sprays* **12**, 721–735.

https://doi.org/10.1017/jfm.2011.298 Published online by Cambridge University Press

DeBar, R. 1974 Fundamentals of the KRAKEN code. *Tech Rep.* UCIR-760. Lawrence Livermore National Laboratory.

Feng, J., Hu, H. H. & Joseph, D. D. 1994 Direct simulation of initial value problems for the motion of solid bodies in a Newtonian fluid. Part 1. Sedimentation. *J. Fluid Mech.* **261**, 95–134.

Haeberle, S., Naegele, L., Zengerle, R. & Durcée, J. 2006 A digital centrifugal droplet-switch for routing of liquids. In *10th International Conference on Miniaturized Systems for Chemistry and Life Sciences, Tokyo, Japan* (ed. T. Kitamori, H. Fujita & S. Hasebe). pp. 570–572. Society for Chemistry and Micro-Nano Systems.

He, M., Edgar, J. S., Jeffries, G. D. M., Lorenz, R. M., Shelby, J. P. & Chiu, D. T. 2005 Selective encapsulation of single cells and subcellular organelles into picoliter- and femtoliter-volume droplets. *Anal. Chem.* **77**, 1539–1544.

Hsiang, L. P. & Faeth, G. M. 1992 Near-limit drop deformation and secondary breakup. *Intl J. Multiphase Flow* **18**, 635–652.

Khan, M. S., Kannangara, D., Shen, W. & Garnier, G. 2008 Isothermal noncoalescence of liquid droplets at the air–liquid interface. *Langmuir* **24**, 3199–3204.

Knupp, P. M. 2003 Algebraic mesh quality metrics for unstructured initial meshes. *Finite Elem. Anal. Des.* **39**, 217–241.

Lamb, H. 1945 *Hydrodynamics*, 6th edn. Dover.

Lee, C. P., Anilkumart, A. V., Hmelo, A. B. & Wang, T. G. 1998 Equilibrium of liquid drops under the effects of rotation and acoustic flattening: results from USML-2 experiments in space. *J. Fluid Mech.* **357**, 43–67.

Lee, C. P., Lyell, M. J. & Wang, T. G. 1985 Viscous damping of the oscillations of a rotating simple drop. *Phys. Fluids* **28** (11), 3187–3188.

Li, Z. L. & Lai, M. C. 2001 The immersed interface method for the Navier–Stokes equations with singular forces. *J. Comput. Phys.* **171**, 822–842.

Loth, E. & Dorgan, A. J. 2009 An equation of motion for particles of finite Reynolds number and size. *Environ. Fluid Mech.* **9**, 187–206.

Lubarsky, E., Reichel, J. R., Zinn, B. T. & McAmis, R. 2010 Spray in crossflow: dependence on Weber number. *Trans. ASME: J. Engng Gas Turbines Power* **132**, 021501.

Osher, S. & Fedkiw, R. P. 2001 Level set methods: an overview and some recent results. *J. Comput. Phys.* **169**, 463–502.

Pearlman, H. G. & Sohrab, S. H. 1991 The role of droplet rotation in turbulent spray combustion modeling. *Combust. Sci. Technol.* **76**, 321–334.

Perot, B. & Nallapati, R. 2003 A moving unstructured staggered mesh method for the simulation of incompressible free-surface flows. *J. Comput. Phys.* **184**, 192–214.

Plateau, J. A. F. 1863 Experimental and theoretical researches on the figures of equilibrium of a liquid mass withdrawn from the action of gravity. In *Annual Report of the Board of Regents of the Smithsonian Institution*, *Washington, DC*, pp. 270–285.

Quan, S. P. 2011 Simulations of multiphase flows with multiple length scales using moving mesh interface tracking with adaptive meshing. *J. Comput. Phys.* **230**, 5430–5448.

Quan, S. P., Lou, J. & Schmidt, D. P. 2009*a* Modeling merging and breakup in the moving mesh interface tracking method for multiphase flow simulations. *J. Comput. Phys.* **228**, 2660–2675.

Quan, S. P. & Schmidt, D. P. 2006 Direct numerical study of a liquid droplet impulsively accelerated by gaseous flow. *Phys. Fluids* **18**, 102103.

Quan, S. P. & Schmidt, D. P. 2007 A moving mesh interface tracking method for 3D incompressible two-phase flows. *J. Comput. Phys.* **221**, 761–780.

Quan, S. P., Schmidt, D. P., Hua, J. & Lou, J. 2009*b* A numerical study of the relaxation and breakup of an elongated drop in a viscous liquid. *J. Fluid Mech.* **640**, 235–264.

Rhim, W. K., Chung, S. K. & Elleman, D. D. 1988 Experiments on rotating charged liquid drops. In *Drops and Bubbles: 3rd Intl Colloq. AIP Conf. Proc. Monterey, CA* (ed. T. G. Wang).

Sethian, J. A. & Smereka, P. 2003 Level set methods for fluid interfaces. *Annu. Rev. Fluid Mech.* **35**, 341–372.

https://doi.org/10.1017/jfm.2011.298 Published online by Cambridge University Press

SON, Y., KIM, C., YANG, D. H. & AHN, D. J. 2008 Spreading of an inkjet droplet on a solid surface with a controlled contact angle at low Weber and Reynolds numbers. *Langmuir* **24**, 2900–2907.

SWAMINATHAN, T. N., MUKUNDAKRISHNAN, K. & HU, H. H. 2006 Sedimentation of an ellipsoid inside an infinitely long tube at low and intermediate Reynolds numbers. *J. Fluid Mech.* **551**, 357–385.

TAN, Z. W., TEO, S. G. G. & HU, J. 2008 Ultrasonic generation and rotation of a small droplet at the tip of a hypodermic needle. *J. Appl. Phys.* **146**, 501–523.

TEMKIN, S. & KIM, S. S. 1980 Droplet motion induced by weak shock waves. *J. Fluid Mech.* **96**, 133–157.

UNVERDI, S. O. & TRYGGVASON, G. 1992 A front-tracking method for viscous, incompressible, multi-fluid flows. *J. Comput. Phys.* **100**, 25–37.

WANG, T. G., ANILKUMART, A. V., LEE, C. P. & LIN, K. C. 1994 Bifurcation of rotating liquid drops: results from USML-1 experiments in space. *J. Fluid Mech.* **276**, 389–403.

WANG, T. G., TRINH, E. H., CROONQUIST, A. P. & ELLEMAN, D. D. 1986 The shape of rotating free drops: Spacelab experimental results. *Phys. Rev. Lett.* **56**, 452–455.

WATANABE, T. 2008 Numerical simulation of oscillations and rotations of a free liquid droplet using the level set method. *Comput. Fluids* **31**, 91–98.

YOUNGREN, G. K. & ACRIVOS, A. 1976 On the shape of a gas bubble in a viscous extensional flow. *J. Fluid Mech.* **76**, 433–442.

YOUNGS, D. L. 1982 Time-dependent multimaterial flow with large fluid distortion. In *Numerical Methods for Fluid Dynamics* (ed. K. W. Morton & M. J. Baines), pp. 273–285. Academic.

ZHANG, X., SCHMIDT, D. & PEROT, B. 2002 Accuracy and conservation properties of a three-dimensional unstructured staggered mesh scheme for fluid dynamics. *J. Comput. Phys.* **175**, 764–791.

ZHENG, H. W., SHU, C. & CHEW, Y. T. 2006 A lattice Boltzmann model for multiphase flows with large density ratio. *J. Comput. Phys.* **218** (1), 353–371.

https://doi.org/10.1017/jfm.2011.298 Published online by Cambridge University Press